

1 **Different effects of anthropogenic emissions and aging processes on the**
2 **mixing state of soot particles in the nucleation and accumulation**
3 **modes**

4

5 Yuying Wang^{1,2}, Rong Hu^{1,2}, Qiuyan Wang¹, Zhanqing Li³, Maureen Cribb³, Yele Sun⁴, Xiaorui
6 Song¹, Yi Shang¹, Yixuan Wu¹, Xin Huang¹, Yuxiang Wang¹

7

8 ¹ Key Laboratory for Aerosol-Cloud-Precipitation of China Meteorological Administration, School
9 of Atmospheric Physics, Nanjing University of Information Science & Technology, Nanjing
10 210044, China

11 ² State Key Laboratory of Remote Sensing Science, College of Global Change and Earth System
12 Science, Beijing Normal University, Beijing 100875, China

13 ³ Earth System Science Interdisciplinary Center, Department of Atmospheric and Oceanic Science,
14 University of Maryland, College Park, MD, USA

15 ⁴ State Key Laboratory of Atmospheric Boundary Layer Physics and Atmospheric Chemistry,
16 Institute of Atmospheric Physics, Chinese Academy of Sciences, Beijing, 100029, China

17

18 Correspondence to: Yuying Wang (yuyingwang@nuist.edu.cn)

19 **Abstract.** In this study, the mixing state of size-resolved soot particles and their influencing factors
20 were investigated based on a five-month aerosol volatility measurement at a suburban site (Xingtai,
21 XT) in the central North China Plain (NCP). The volatility and mixing state of soot-containing
22 particles at XT were complex caused by multiple pollution sources and various aging processes.
23 The results suggest that anthropogenic emissions can weaken the mean volatility of soot-containing
24 particles and enhance their degree of external mixing. There were fewer externally mixed soot
25 particles in warm months (June, July, and August) than in cold months (May, September, and
26 October). Monthly variations in the mean coating depth ($D_{c,mean}$) of volatile matter on soot particles
27 showed that the coating effect was stronger in warm months than in cold months, even though
28 aerosol pollution was heavier in cold months. Moreover, the volatility was stronger, and the degree
29 of internal mixing was higher in nucleation-mode soot-containing particles than in accumulation-
30 mode soot-containing particles. Relationships between $D_{c,mean}$ and possible influencing factors
31 [temperature (T), relative humidity (RH), and particulate matter with diameters ranging from 10 to
32 400 nm] further suggest that high ambient T and RH in a polluted environment could promote the
33 coating growth of accumulation-mode soot particles. However, high ambient T but low RH in a
34 clean environment were beneficial to the coating growth of nucleation-mode soot particles. Our
35 results highlight the diverse impact of anthropogenic emissions and aging processes on the mixing
36 state of soot particles in different modes, which should be considered separately in models to
37 improve the simulation accuracy of aerosol absorption.

39 1. Introduction

40 Aerosols are mixed liquid and solid particles suspended in the atmosphere. Some aerosols are
41 directly produced from natural or anthropogenic sources (i.e., primary aerosols), and the rest are
42 indirectly transformed from gas precursors through atmospheric chemical reactions (i.e., secondary
43 aerosols). The newly formed particles can grow or shrink through various aging processes (e.g.,
44 condensation, coagulation, volatilization, chemical reactions). Aerosol physicochemical properties
45 (number concentration, shape, mixing state, optical properties, among others) are thus highly
46 variable. This is one of the reasons why aerosols are highly uncertain in climate change assessments
47 (Bond et al., 2013; Seinfeld et al., 2016; Bellouin et al., 2020; Christensen et al., 2021). Although
48 great efforts have been made to understand aerosol optical properties, the uncertainty of radiative
49 forcing caused by aerosols is still two to three times that of greenhouse gases (IPCC, 2021).

50 Aerosols can affect the earth-atmosphere radiation balance by scattering or absorbing shortwave
51 and longwave radiation, which is called the aerosol direct climate effect or aerosol-radiation
52 interactions. Many factors, such as aerosol chemical composition, mixing state, and ambient relative
53 humidity (RH), have complex impacts on aerosol-radiation interactions (e.g., Twohy et al., 2009;

54 Kuniyal and Guleria, 2019; Ren et al., 2021). According to the sixth IPCC report, the total direct
55 radiative forcing caused by anthropogenic aerosols is generally negative. However, light-absorbing
56 carbonaceous particles (LAC) have a warming effect on climate (Ramana et al., 2010; Gustafsson
57 and Ramanathan, 2016), which can partly offset the cooling effect caused by scattering aerosols,
58 such as sulfate. Black carbon (BC) is the most important LAC compound, ~~mostly emitted as soot
59 from anthropogenic sources (incomplete fossil fuel combustion and biomass burning) (Novakov et
60 al., 2003).~~ Some experiments have suggested that BC in urban polluted environments can play an
61 important role in pollution formation and development. The internal mixing of BC with secondly
62 formed matter could also greatly enhance light absorption (Peng et al., 2016; Zhou et al., 2017).
63 Moreover, BC is mostly emitted as soot from anthropogenic sources (incomplete fossil fuel
64 combustion and biomass burning) (Novakov et al., 2003). ~~—Soot particles are abundant in both
65 nucleation and accumulation modes (Li et al., 2011; Levy et al., 2013; La Rocca et al., 2015; Hu et
66 al., 2021; Zhang et al., 2021).~~

67 The online measurement instruments quantifying the mixing state of BC-containing particles are
68 limited. Based on the measurement of single-particle soot photometer (SP2), Wu et al. (2017)
69 indicated that the mass of refractory black carbon (*r*BC) had an approximately lognormal
70 distribution as a function of the volume-equivalent diameter (VED) in Beijing. Yu et al. (2020)
71 suggested that the mixing state of *r*BC particles was related to air pollution levels and air mass
72 sources. Zhang et al. (2021) further indicated that meteorological conditions had a large impact on
73 the mixing state of *r*BC particles. Moreover, the Aerodyne soot particle aerosol mass spectrometer
74 (SP-AMS) can also be used to study the mixing state of *r*BC. For example, J. Wang et al. (2019)
75 found that the formation of secondary aerosols through photochemical and aqueous chemical
76 reactions was responsible to the coating of *r*BC based on the measurement of SP-AMS in winter
77 Beijing. However, the lower observation limit of particle size by SP2 and SP-AMS is larger than
78 ~70 nm. Therefore, they cannot quantify the mixing state of BC-containing particles in the small
79 nucleation mode. ~~Modern gasoline direct injection (GDI) vehicles can emit plentiful ultrafine BC-
80 containing (soot) particles in the ambient (La Rocca et al., 2015; Hu et al., 2021). The tiny soot
81 particles embedded in other material (such as sulfate) play a significant role in particle growth (Li
82 et al., 2011). Investigating the mixing state of BC-containing particles and their factors in different
83 modes are needed.~~

84 Aerosol volatility refers to the shrinking extent of particles at a certain temperature. The mixing
85 state of soot particles or tarballs is closely related to aerosol volatility at high temperatures (Philippin
86 et al., 2004; Wehner et al., 2009; Adachi et al., 2018, 2019). Most primary soot particles from
87 anthropogenic sources are refractory, hydrophobic, and externally mixed. In a polluted environment,
88 primary soot particles are easily transformed to internally mixed particles through certain coating

89 processes in the atmosphere (Cheng et al., 2012; Peng et al., 2016; F. Zhang et al., 2020). However,
90 coating matter is generally non-refractory because most of the matter consists of secondary chemical
91 species, such as organics, sulfate, and nitrate (Philippin et al., 2004; Hong et al., 2017). This is why
92 aerosol volatility can characterize the mixing state of soot particles in polluted environments
93 (Wehner et al., 2009; Hossain et al., 2012; S. Zhang et al., 2016). A volatility tandem differential
94 mobility analyzer (VTDMA) is usually used to quantify aerosol volatility by measuring the change
95 in particle size at a set temperature. Aerosol volatility measured by a VTDMA at a high temperature
96 ($> 280^{\circ}\text{C}$) can be used to study the mixing state of soot particles (Philippin et al., 2004; Wehner et
97 al., 2009; Y. Zhang et al., 2016; Wang et al., 2017). Meanwhile, VTDMA measurements are based
98 on the aerosol number concentration, which is always high in the nucleation mode in the ambient.
99 Therefore, VTDMA can quantify the mixing state of nucleation-mode soot particles.

100 Over the past years, several studies have reported the volatility and mixing state of particles based
101 on VTDMA measurements in the North China Plain (NCP). For example, Wehner et al. (2009)
102 found that the mixing state of soot particles in Beijing and its surrounding region varied, especially
103 between new particle formation days and heavily polluted days. Using the same VTDMA and
104 aerosol optical data, Cheng et al. (2009) conducted an aerosol optical closure study, finding that soot
105 aging was rapid at the Yufa site south of Beijing. The coating on soot particles can enhance aerosol
106 absorption and scattering coefficients by a factor of 8 to 10 within several hours due to secondary
107 processing during the daytime, which is the combined effect of the increased thickness of the coating
108 shell and the transition of soot from an externally mixed state to a coated state. Cheng et al. (2012)
109 further indicated that aging and emissions were two competing factors in the mixing state of soot
110 particles. Based on VTDMA measurement data collected in 2015, Wang et al. (2017) indicated that
111 strict emission control measures implemented in Beijing and surrounding areas could enhance the
112 volatility of soot-containing particles and their degrees of external mixing. At another regional site
113 (Xianghe) in the northern part of the NCP, S. Zhang et al. (2016) found that the mixing state of
114 ambient particles was complex with different volatilities. Furthermore, Y. Zhang et al. (2016)
115 suggested that the average shell-to-core ratio and absorption enhancement (E_{ab}) of ambient BC was
116 2.1–2.7 and 1.6–1.9, respectively.

117 These studies imply that anthropogenic emissions play an important role in the volatility and
118 mixing state of soot-containing particles and that the coating on soot particles can greatly enhance
119 aerosol absorption. However, these studies were based on data collected during short-term
120 observational periods in the northern part of the NCP and they did not distinguish the factors
121 influencing the mixing state of nucleation- and accumulation-mode soot particles. Recent studies
122 (Y. Wang et al., 2018, 2019, 2021) have shown that anthropogenic sources and aerosol aging
123 processes are various in the north and central-south NCP, leading to diverse aerosol physiochemical

124 properties between these regions in different seasons. More research about the mixing state of soot
125 particles in the central-south NCP is needed to improve the accuracy of modeled aerosol optical
126 properties.

127 This study investigates for the first time the volatility and mixing state of nucleation- and
128 accumulation-mode soot-containing particles in the warm and cold seasons based on one
129 comprehensive field campaign that took place in the central NCP, lasting five months. Exploring
130 factors influencing the volatility and mixing state of soot-containing particles in this study will
131 improve the accuracy of modeled aerosol optical properties in the central NCP. This paper is
132 organized as follows. Section 2 introduces the sampling site, instruments, and data analysis. Section
133 3 presents the results and discussion, including meteorological conditions, aerosol pollution levels,
134 changes in volatility and mixing state of soot-containing particles, and their influencing factors.
135 Section 4 gives conclusions and summarizes the study.

136

137 2. Sampling site, instruments, and data analysis

138 2.1 Sampling site

139 Data used in this study were collected at the National Meteorological Basic Station ($37^{\circ}11'N$,
140 $114^{\circ}22'E$, 180 m above sea level) in Xingtai (XT), China, equipped with a variety of meteorological
141 observation instruments. The measured meteorological variables including ambient temperature,
142 relative humidity (RH), wind direction and speed were used in this study. Y. Wang et al. (2018)
143 reported that this site was located in a polluted area of the central-south NCP, influenced by multiple
144 anthropogenic sources, such as industrial coal firing, fossil-fuel burning, agricultural activities, and
145 household emissions. The long-distance transport of pollutants also influences the air quality at XT.
146 Previous studies have suggested that air pollution at XT represents well regional pollution
147 characteristics in the central NCP, east of the Taihang Mountains (Y. Zhang et al., 2018; Y. Wang
148 et al., 2018). A comprehensive field campaign named the Atmosphere-Aerosol-Boundary layer-
149 Cloud (A²BC) Interaction Joint Experiment was carried out at XT from May to October of 2016. Y.
150 Wang et al. (2018) and Li et al. (2019) provide details about the XT site and the A²BC campaign.
151 Here, over five months of aerosol observational data, including particle number size distribution
152 (PNSD), aerosol volatility, and BC mass concentration, were used to analyze the volatility and
153 mixing state of soot particles and their influencing factors.

154

155 2.2 Instruments

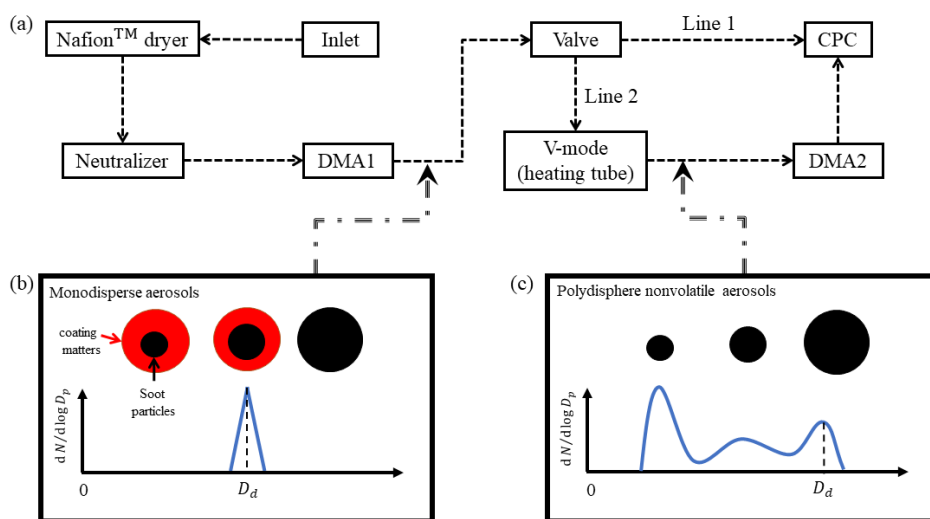
156 2.2.1 Measuring PNSD and aerosol volatility

157 The tandem differential mobility analyzer (TDMA) system is widely used to measure the change
158 in particle size under special conditions, e.g., high humidity, high temperature, and chamber

159 chemical reactions (Swietlicki et al., 2008). In this campaign, the VTDMA system was used to
 160 measure aerosol volatility at 300°C. The inlet air sample was first dried by a Nafion™ dryer to low
 161 RH (< 30%), then neutralized by a soft X-ray neutralizer (model 3088, TSI Inc.; Fig. 1a). Afterwards,
 162 quasi-monodisperse aerosols (Fig. 1b) with a certain dried diameter (D_d) were split by the first
 163 differential mobility analyzer (DMA1). In this campaign, D_d was set to 40, 80, 110, 150, 200, and
 164 300 nm. An automated valve located after the DMA1 had two outlet lines. Line 1 directly accessed
 165 the water-based condensation particle counter (WCPC, model 3787, TSI Inc.), measuring the
 166 number concentration of particles ranging from 10 to 400 nm. Line 2 accessed a heating tube,
 167 vaporizing volatile materials at a controlled high temperature (300°C in this study). The ratio of
 168 particle size after volatilization [$D_p(T)$] to D_d is defined as the aerosol shrink factor (i.e., $SF = D_p(T)$
 169 / D_d). After heating, residual aerosols were generally polydisperse nonvolatile particles (Fig. 1c).
 170 The second DMA (DMA2) and WCPC were used to measure the number size distribution of
 171 nonvolatile particles, measuring the distribution function of SF (SF -MDF). Finally, the probability
 172 density function of SF (SF -PDF) was retrieved using the TDMAfit algorithm (Stolzenburg and
 173 McMurry, 1988; Stolzenburg and McMurry, 2008).

174 In this study, we assume that the shape of all particles follows the core-shell model (nonvolatile
 175 core and volatile shell; Fig. 1b). Residual particles after volatilization have different-sized
 176 nonvolatile cores (Fig. 1c). Previous studies have suggested that residual particles at 300°C mainly
 177 consist of soot (Philippin et al., 2004; Wehner et al., 2009). Aerosol volatility measured by the
 178 VTDMA in this study can thus reflect the degree of mixing state of soot particles.

179



180

181 **Figure 1.** Schematic diagram of the volatility tandem differential mobility analyzer used in this
 182 study.

183

184 2.2.2 Measuring BC

185 In this campaign, a seven-wavelength aethalometer (model AE-33, Magee Scientific Corp.) was
186 used to measure the mass concentration of BC (M_{BC}). After calibration, the sampling flow rate of
187 the AE-33 was 5.0 L min^{-1} . A cyclone with particulate matter (diameters = $2.5 \text{ }\mu\text{m}$, or $\text{PM}_{2.5}$) was
188 used in the sample inlet. Aerosol particles were collected on filter tape through a spot, and the
189 instantaneous concentration of optically absorbing aerosols was retrieved from the rate of change
190 of the attenuation of light transmitted through the filter. The wavelength channels of the AE-33 were
191 370, 470, 525, 590, 660, 880, and 940 nm. According to the manufacturer's instructions, the M_{BC} is
192 calculated from the change in optical attenuation at channel 6 (i.e., 880 nm) in the selected time
193 interval using the mass absorption cross section (MAC) of $7.77 \text{ m}^2 \text{ g}^{-1}$. The dependency of MAC on
194 BC coating may introduce some uncertain in calculating MAC (Drinovec et al., 2015).

195

196 2.2.3 VTDMA data analysis

197 The retrieved SF -PDF ($c(D_d, SF)$) is normalized as $\int c(D_d, SF) dSF = 1$. The ensemble mean
198 shrink factor (SF_{mean}) is then calculated as

$$199 SF_{\text{mean}}(D_d) = \int_0^{\infty} SF \cdot c(D_d, SF) dSF . \quad (1)$$

200 Particles can be classified into several volatile groups according to different SF ranges (Y.
201 Wang et al., 2017). The number fraction (NF) for each volatile group with the SF boundary of $[a, b]$
202 is calculated as

$$203 NF(D_d) = \int_a^b c(D_d, SF) dSF . \quad (2)$$

204 Based on the core-shell assumption, the coating depth (D_c) of soot particles is defined as the
205 depth of shell materials (i.e., shell depth). According to the definition of SF , D_c for the particle
206 (D_d, SF) can be calculated as

$$207 D_c(D_d, SF) = \frac{D_d}{2} (1 - SF). \quad (3)$$

208 The ensemble mean D_c ($D_{c,\text{mean}}$) using the normalized SF -PDF data is then calculated as

$$209 D_{c,\text{mean}}(D_d) = \int_0^{\infty} D_c(D_d, SF) \cdot c(D_d, SF) dSF. \quad (4)$$

210

211 3. Results and discussion

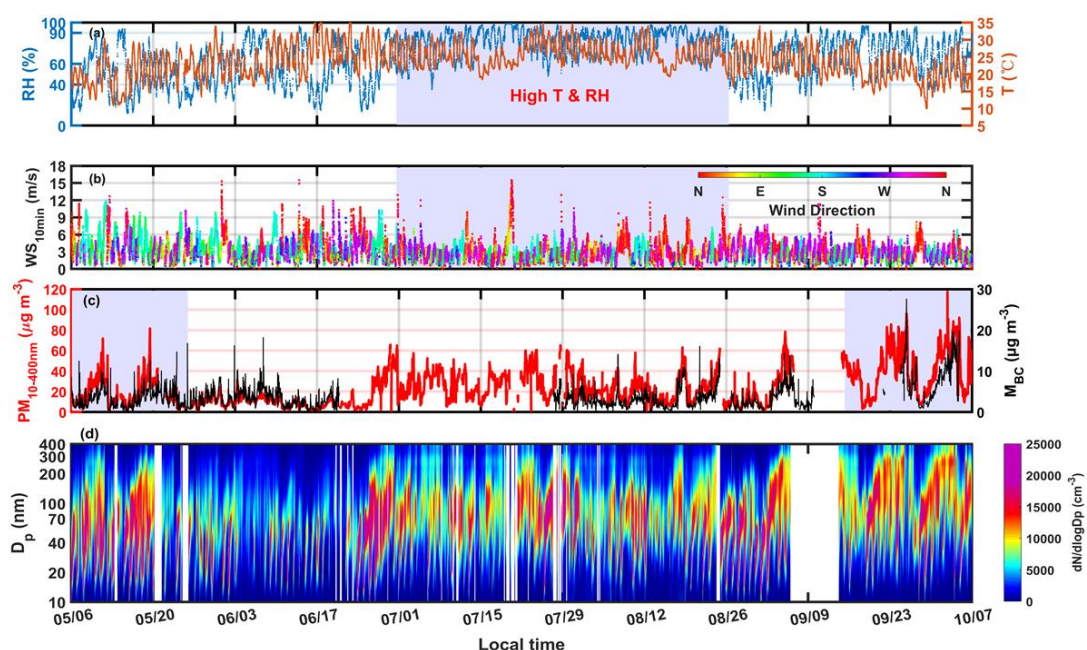
212 3.1 Meteorological conditions and aerosol pollution levels

213 Figure 1a-b shows the time series of ambient temperature (T), RH, and wind direction and
214 speed (WD and WS, respectively) during the campaign. Monthly changes in T are clearly seen (Fig.
215 2a). Average T s in warm (June, July, and August) and cold (May, September, and October) months

216 were 25.73 ± 3.80 and 19.0 ± 5.74 °C, respectively. The meteorological variables changed periodically
 217 in cold months but not in warm months, which is caused by the cold fronts in cold months. Figure
 218 2a also suggests that RH was higher in July and August than in other months.

219 Figure 2b shows that the wind changed significantly in different months at XT. Monthly wind
 220 rose diagrams (Fig. S1) indicate that northwest winds prevailed in all months, caused by the special
 221 terrain around XT (Y. Zhang et al., 2018). In July, weak southeast winds were also present,
 222 beneficial to the accumulation of air pollutants due to the stable atmospheric environment. In August,
 223 the other prevailing wind was from the north, which was beneficial for atmospheric diffusion.

224



225

226 **Figure 2.** Time series of (a) ambient relative humidity (RH; unit: %), and temperature (T ; unit: °C),
 227 (b) wind direction (WD) and 10-minute-averaged wind speed (WS; unit: m s^{-1}), (c) mass
 228 concentration of 10–400 nm particles (PM_{10-400} , in red; unit: $\mu\text{g m}^{-3}$), assuming that the aerosol
 229 density is 1.6 g cm^{-3} , and mass concentration of black carbon (M_{BC} , in black; unit: $\mu\text{g m}^{-3}$), and (d)
 230 particle number size distribution at the Xingtai site from 6 May 2016 to 6 October 2016.

231

232 In this study, the total mass concentration of 10–400-nm particles (PM_{10-400}) (Fig. 2c) was
 233 calculated using PNSD data (Fig. 2d), assuming that the aerosol density was 1.6 g cm^{-3} (Y. Wang
 234 et al., 2017). The average PM_{10-400} concentrations in warm and cold months were 19.68 ± 13.58 and
 235 $29.79 \pm 21.37 \mu\text{g m}^{-3}$, respectively, indicating much higher aerosol pollution in cold months than in
 236 warm months. In cold months, PM_{10-400} accumulated periodically as accumulation-mode ($D_p > 100$
 237 nm) particles increased. This is closely related to cyclic changes in general atmospheric circulation,
 238 reflected by the cycle of winds (Fig. 2b). However, PM_{10-400} was lower in May than in September
 239 and October, likely due to the weaker particle growth in May. During warm months, PM_{10-400}

240 reached its lowest value in June with the lowest number concentration of accumulation-mode
241 particles of all months (Fig. S2), suggesting that meteorological conditions in June were not
242 conducive to particle growth. The high T and RH in July and August were beneficial to particle
243 growth by promoting atmospheric photochemical and liquid chemical reactions (Z. Wu et al., 2018;
244 Peng et al., 2021). Figure 2c suggests that PM_{10-400} was much higher in July and August than in June,
245 although the mass concentrations of black carbon (M_{BCS}) in these months were considerable.
246 However, PM_{10-400} was lower in August than in July, likely because of the better atmospheric
247 diffusion conditions (more and stronger northerly winds) in August. Figure 2c also shows that
248 changes in M_{BC} and PM_{10-400} were similar, suggesting the possible role of BC in the formation
249 processes of aerosol pollution. Recently, F. Zhang et al. (2020) demonstrated that BC-catalyzed
250 sulfate formation involving NO_2 and NH_3 plays an important role in the formation of haze events.

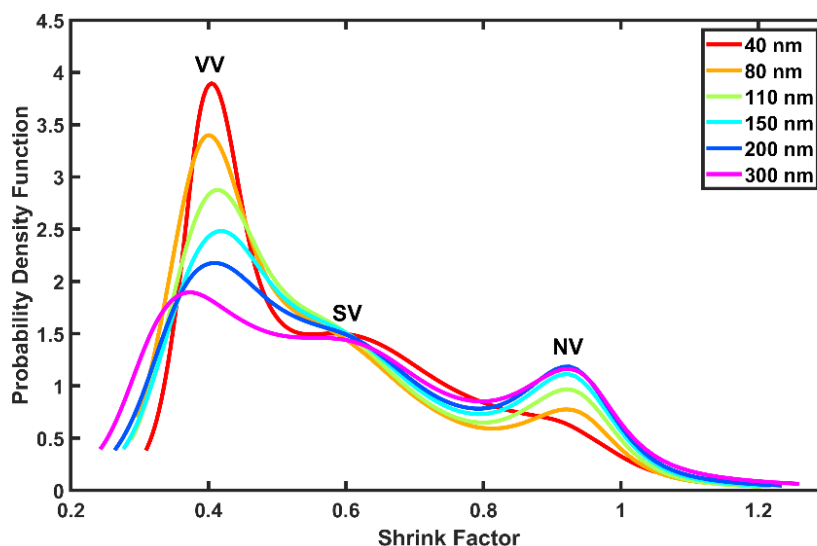
251

252 3.2 Monthly and diurnal variations in SF -PDF

253 Figure 3 shows the size-resolved mean SF -PDFs at XT. In general, SF -PDFs had three peak
254 modes, namely, at $SF \approx 0.4$ [very volatile (VV) mode], 0.6 [slightly volatile (SV) mode], and 0.9
255 [nonvolatile (NV) mode]. The trimodal distributions of SF -PDFs at XT in the central NCP differ
256 from those at sites in the northern NCP (S. Zhang et al., 2016; Y. Wang et al., 2017), implying
257 highly complex volatility and mixing state of soot particles at XT. Note that the SF -PDF of 40-nm
258 particles has a quasi-unimodal distribution pattern peaked at VV mode, with low fractions of NV-
259 and SV-mode particles. This means that the residual soot size of most 40-nm particles after heating
260 at 300°C was about 16 nm. These tiny soot particles are mainly from anthropogenic sources such
261 as vehicle emissions (La Rocca et al., 2015; Hu et al., 2021). Extremely low-volatile organics are
262 another possible component in this size. However, these extremely low-volatile organics are
263 mainly formed in the forest area (Ehn et al., 2014). XT is located in the severe polluted area with
264 kinds of anthropogenic sources. It is expected that there are many nucleation-mode soot particles
265 in the ambient in this region. ~~In addition, p~~Previous studies have indicated that most NV-mode
266 particles are externally mixed soot particles (Cheng et al., 2012; Cheung et al., 2016). This
267 suggests that soot-containing particles in nucleation mode (represented by 40-nm particles) in this
268 study had strong volatility and a high degree of internal mixing. ~~These tiny soot particles in~~
269 ~~nucleation mode are mainly from modern vehicle emissions (La Rocca et al., 2015; Hu et al.,~~
270 ~~2021).~~

271 Figure 3 also suggests that the fraction of NV-mode particles increased with increasing
272 particle size, indicating a higher fraction of externally mixed soot particles in accumulation mode.
273 This is related to the primary size of soot particles. Some studies suggest that most freshly emitted
274 refractory particles (like BC) are primarily in accumulation mode. For example, Levy et al. (2013)

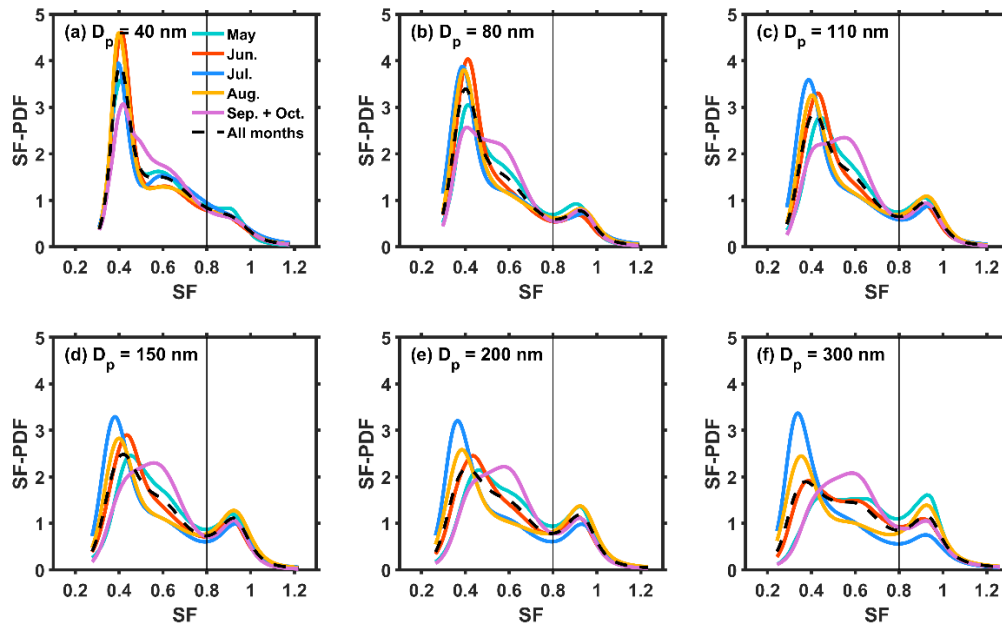
275 reported that fresh BC was mostly in the 150–240 nm size range, while Wu et al. (2017) reported
276 that refractory BC size distribution measurements in Beijing peaked at about 200 nm, with a
277 secondary less significant mode at about 600 nm.
278



279
280 **Figure 3.** Size-resolved mean probability density functions of the shrink factor at different
281 wavelengths. VV stands for “very volatile”, SV stands for “slightly volatile”, and NV stands for
282 “non-volatile”.
283

284 Figure 4a-b shows that VV-mode fractions in the *SF*-PDFs of 40-nm and 80-nm particles were
285 higher in warm months than in cold months, indicating that nucleation-mode soot particles were
286 more volatile in warm months. Our previous study has shown that new particle formation (NPF)
287 events occurred frequently at XT (Y. Wang et al., 2018). Wehner et al. (2009) reported that most
288 newly formed matter is composed of organics and sulfate, easily volatilized at 300°C. Li et al. (2011)
289 indicated that the tiny soot particles embedded in sulfates could promote particle growth during NPF
290 events in the NCP. All this implies that coating by newly formed secondary matter was the possible
291 reason for the high volatility of nucleation-mode soot-containing particles in warm months. For
292 accumulation-mode (110–300 nm) particles (Fig. 4c-f), monthly changes in *SF*-PDF patterns are
293 clearly seen. In general, *SF* peak values of the VV mode were smaller (meaning a thicker coating of
294 volatile matter), and fractions of VV-mode particles were higher in warm months (especially in July)
295 than in cold months, indicating that the coating on accumulation-mode soot particles was also
296 stronger in warm months than in cold months. As previously mentioned, meteorological conditions
297 in warm months (i.e., high *T* and RH) were favorable to the particle growth of soot particles through
298 atmospheric photochemical and liquid chemical reactions. In cold months (May, September, and
299 October), the volatility of accumulation-mode soot-containing particles was relatively lower,
300 indicating thinner coating matter on the surfaces of soot particles in the polluted cold environment.

301 This is consistent with measurements made at an urban site in Beijing (Yu et al., 2020). Yu et al.
 302 (2020) also suggests that a more even distribution of *r*BC and non-*r*BC material mass fractions in
 303 summer than in winter, which may be caused by higher amount of secondary material.
 304

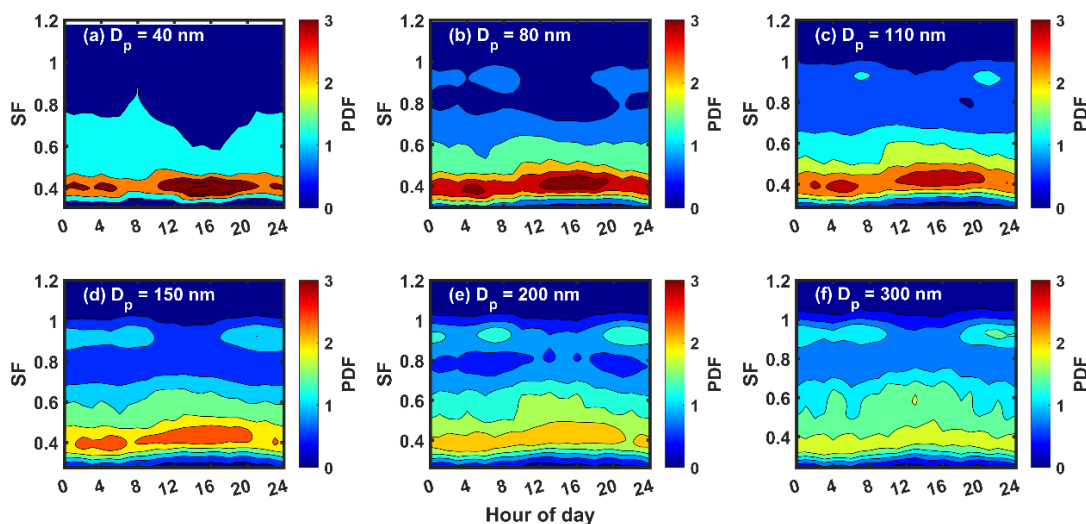


305
 306 **Figure 4.** Monthly variations in the mean shrink factor (*SF*) probability distribution functions (*SF*-
 307 PDFs) for particles with diameters of (a) 40 nm, (b) 80 nm, (c) 110 nm, (d) 150 nm, (e) 200 nm,
 308 and (f) 300 nm.

309
 310 Figure 5 shows diurnal variations in *SF*-PDF for different size particles, illustrating the distinct
 311 diurnal variation patterns of *SF*-PDF for nucleation- and accumulation-mode particles. VV-mode
 312 fractions for 40-nm and 80-nm particles ($\sim SF = 0.4$) increased sharply from around noon into the
 313 afternoon (Fig. 5a-b). Figure S3 shows that the number concentration of 40-nm and 80-nm particles
 314 increased quickly due to the influence of NPF events. This further corroborates that newly formed
 315 particles created during NPF events are the possible coating matter on nucleation-mode soot
 316 particles. Figure 5c-f suggests that NV-mode fractions in accumulation-mode soot particles ($\sim SF =$
 317 0.9) were higher than those in nucleation-mode soot particles and that these fractions became higher
 318 with increasing particle size. NV-mode fractions in accumulation-mode soot particles clearly
 319 increased during the morning and evening rush hours. This suggests that anthropogenic emissions
 320 have a large impact on the volatility and mixing state of soot particles, especially for accumulation-
 321 mode soot particles. Previous studies have shown that some of the primary pollutants generated by
 322 human activities are composed of refractory materials, such as BC (Philippin et al., 2004; Levy et
 323 al., 2014). An increase in primary refractory particles could weaken the ensemble volatility and
 324 mixing state of soot particles. Figure 3c-f also shows that the NV-mode fraction in the *SF*-PDF of

325 accumulation-mode particles decreased sharply in the daytime, likely caused by the coating effect
326 of volatile matter through photochemical reactions.

327



328

329 **Figure 5.** Diurnal variations in size-resolved shrink factor (*SF*) probability distribution functions
330 (PDFs) for particles with diameters of (a) 40 nm, (b) 80 nm, (c) 110 nm, (d) 150 nm, (e) 200 nm,
331 and (f) 300 nm.

332

333 In summary, the volatility and mixing state of soot-containing particles were complex at XT
334 during the field campaign. Soot-containing particles in the nucleation mode had strong volatility
335 and a high degree of internal mixing, likely due to the impact of frequent NPF events that occurred
336 during this campaign. The strong volatility and high degree of internal mixing in warm months were
337 likely caused by the aging processes of particles. Anthropogenic emissions also had a large impact
338 on the volatility and mixing state of soot particles, especially in the accumulation mode. The impacts
339 of anthropogenic emissions and secondary chemical reactions on the volatility and mixing state of
340 soot particles will be further discussed next.

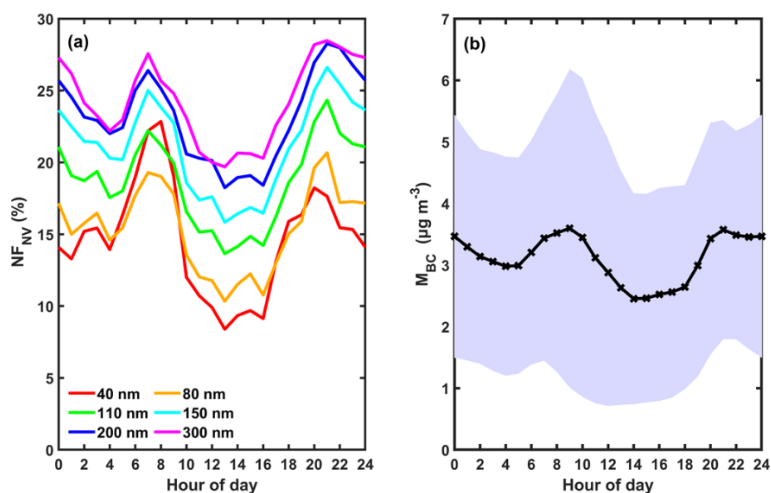
341

342 3.3 Factors influencing the volatility and mixing state of soot particles

343 3.3.1 The impact of anthropogenic emissions on the volatility and mixing state of soot 344 particles

345 As previously discussed, soot particles from anthropogenic emissions were always refractory and
346 nonvolatile at 300°C. Analyzing the relationship between the number fraction of nonvolatile-mode
347 particles (NF_{NV} , $SF > 0.8$) in *SF*-PDFs and M_{BC} can verify this because BC is the main matter in
348 soot particles. Figure 6a shows that NF_{NV} reached two peak values, one during the morning rush
349 hour at about 08:00 and the other during the evening rush hour at about 20:00. M_{BC} also reached

350 two peak values at those same times (Fig. 6b). Overall, the diurnal variation trends of NF_{NV} for all
 351 sizes and M_{BC} were similar. This suggests the great impact of anthropogenic BC on the volatility
 352 and mixing state of soot particles. NF_{NV} decreased quickly after rush hours, especially in the
 353 morning (Fig. 6a), suggesting that the aging processes of primary soot particles were quick at this
 354 heavily polluted site. Cheng et al. (2012) also observed the same phenomenon at a suburban site in
 355 Beijing.



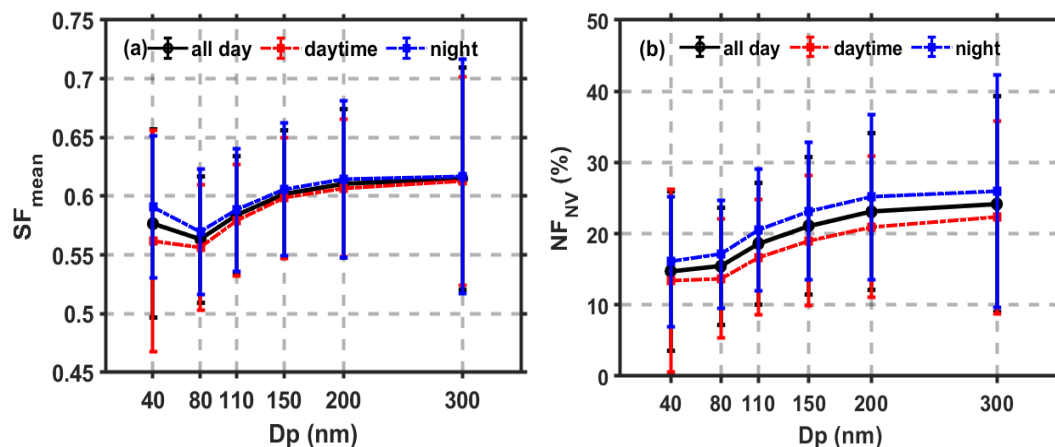
356
 357 **Figure 6.** Diurnal variations in (a) wavelength-dependent, size-resolved number fractions of
 358 nonvolatile particles (NF_{NV}), and (b) mass concentration of black carbon (M_{BC}). The purple,
 359 shaded area shows the standard deviations of M_{BC} .

360

361 3.3.2 The impact of aging processes on the volatility and mixing state of soot-containing 362 particles

363 Lower SF_{mean} values mean stronger aerosol volatility, indicating a larger coating depth of volatile
 364 matter on soot particles. Figure 7a suggests that volatility is stronger during daytime than at night
 365 (i.e., a lower SF_{mean}), particularly for 40-nm particles. This illustrates the large impact of
 366 photochemical reactions on the volatility and mixing state of soot particles. Figure 7a also suggests
 367 that the SF_{mean} of 80-nm particles was lower than that of 40-nm particles. Wang et al. (2018) suggests
 368 that aerosol hygroscopicity of 40-nm particles is larger than that of 80-nm particles during the
 369 daytime at this site. These indicate the great impact of photochemical reactions on the
 370 physicochemical properties of nucleation-mode particles. Inversely, SF_{mean} increased with
 371 increasing particle size in the accumulation mode (110–300 nm), suggesting weaker volatility and
 372 a smaller coating depth for larger accumulation-mode soot particles.

373



374

375 **Figure 7. (a)** Size-resolved ensemble mean shrink factors (SF_{mean}) and **(b)** size-resolved number
 376 fractions of nonvolatile particles (NF_{NV}) during the 24-hr day (black solid lines), during daytime
 377 (red dotted lines), and during nighttime (blue dotted lines). The error bars denote standard deviations.

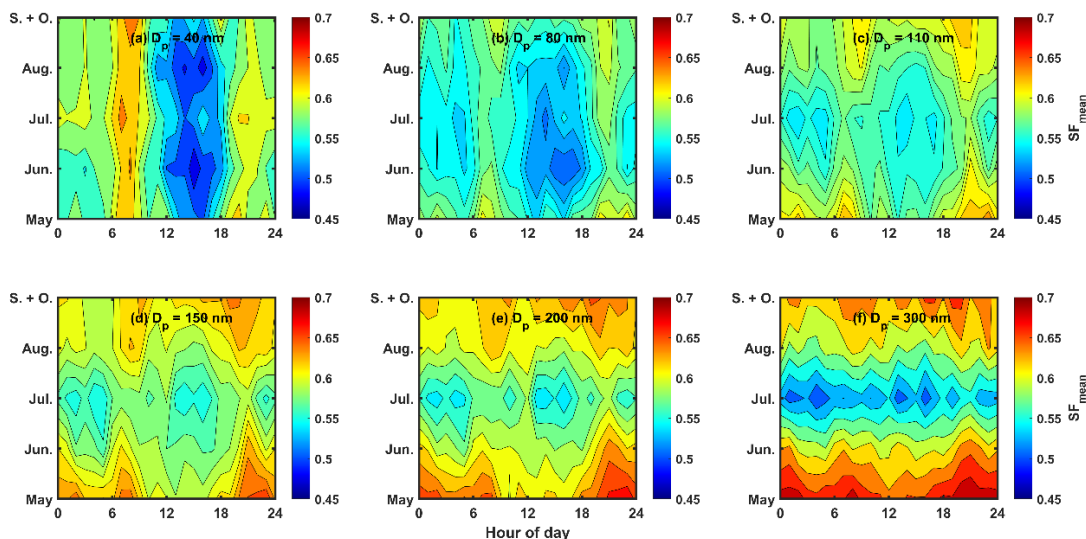
378 Figure 8 shows the diurnal variation in SF_{mean} in different months for different particle sizes.
 379 Figure 8a-b shows that the SF_{mean} of 40-nm and 80-nm particles clearly increased during the
 380 morning and evening rush hours in all months. However, the SF_{mean} of 40-nm and 80-nm particles
 381 decreased sharply in the afternoon. This suggests that the volatility of nucleation-mode soot-
 382 containing particles was easily influenced by anthropogenic emissions during rush hours and
 383 photochemical reactions in the daytime. The diurnal variation patterns of SF_{mean} (Fig. 8c-f) in the
 384 accumulation mode were diverse in different months. The SF_{mean} in warm months was usually lower
 385 than in cold months, indicating a larger impact of aging processes on the volatility of accumulation-
 386 mode soot-containing particles in warm months. Figure 8c-f also shows that the SF_{mean} in
 387 accumulation mode was lowest in July. This suggests that high T , high RH, and the stable
 388 atmospheric environment in July were conducive to the coating of secondary matter on
 389 accumulation-mode soot particles, a possible reason for the high aerosol pollution levels in July.
 390 Moreover, Fig. 8 suggests that monthly variations in SF_{mean} became larger with increasing particle
 391 size. The seasonal variation in the coating effect should thus be considered when modeling
 392 physicochemical properties of soot particles, especially larger particles.

393 To further investigate the impact of aging processes on the mixing state of soot particles, size-
 394 resolved NF_{NV} in the daytime and at night were compared (Fig. 7b). NF_{NV} was always lower in the
 395 daytime than at night, meaning that the fraction of externally mixed soot particles in the daytime
 396 was lower. This further indicates that photochemical reactions in the daytime can transform
 397 externally mixed soot particles into internally mixed soot particles. Figure 7b also shows that NF_{NV}
 398 increased with increasing particle size, meaning a higher degree of external mixing of larger
 399 particles. This suggests that the degree of external mixing was higher for accumulation-mode soot
 400 particles than nucleation-mode particles.

401 The diurnal variation patterns of NF_{NV} (Fig. S4) and SF_{mean} (Fig. 8) in different months were
 402 similar. Externally mixed soot particles increased during the morning and evening rush hours due
 403 to enhanced anthropogenic emissions. Monthly differences in NF_{NV} increased with increasing
 404 particle size. Figure S4 also shows a lower number fraction of externally mixed soot particles (i.e.,
 405 a smaller NF_{NV}) in warm months than in cold months.

406 These results illustrate the distinct volatilities and mixing states of soot particles between the
 407 nucleation and accumulation modes. A lower degree of external mixing and thicker coating depth
 408 in nucleation-mode particles exists. It is thus important to quantify the impact of the coating effect
 409 for nucleation-mode soot particles when studying aerosol physicochemical properties. The next
 410 section analyzes the coating depth and its influencing factors.

411



412

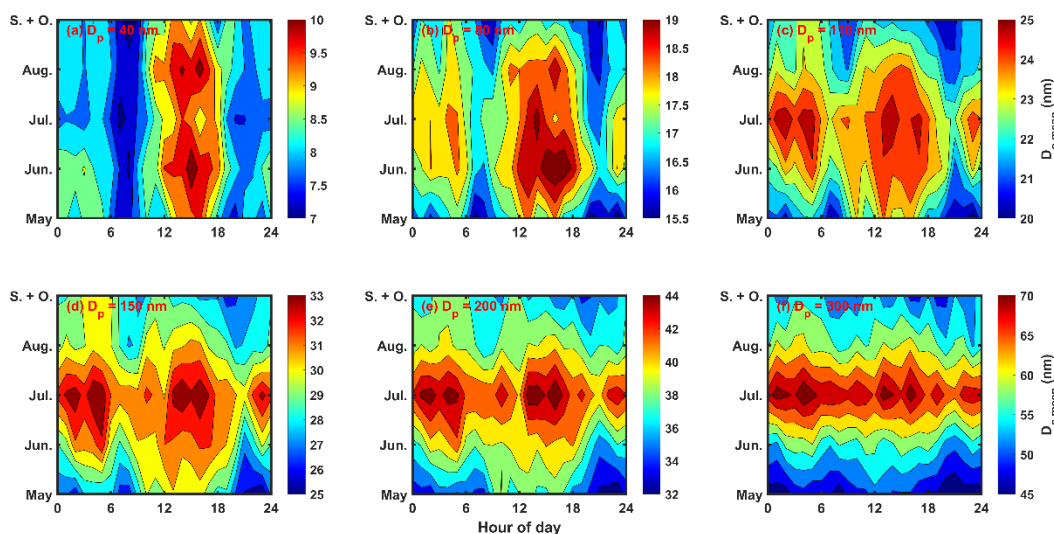
413 **Figure 8.** Diurnal variations in ensemble mean shrink factor (SF_{mean}) in different months for
 414 different particle sizes.

415

416 3.4 The coating depth of secondary matter on soot particles

417 The ensemble mean coating depth on soot particles ($D_{c,mean}$) can be calculated using Eq. (4).
 418 Figure 9 shows diurnal variations in $D_{c,mean}$ in different months for different particle sizes. The
 419 diurnal variation patterns of $D_{c,mean}$ for nucleation-mode and accumulation-mode soot particles
 420 differ greatly. The diurnal variation patterns of $D_{c,mean}$ in different months were similar for
 421 nucleation-mode soot particles (40-nm and 80-nm particles) but not for accumulation-mode soot
 422 particles (110–300-nm particles). The enhancement of $D_{c,mean}$ in the daytime occurred in all months
 423 for nucleation-mode soot particles but only in the warm months for accumulation-mode soot
 424 particles. At night, the enhancement of $D_{c,mean}$ for accumulation-mode soot particles was strong,
 425 especially in warm months. However, it was weak for nucleation-mode soot particles. These all

426 imply large differences in $D_{c,mean}$ in different months for nucleation-mode and accumulation-mode
 427 soot particles, likely caused by variations in meteorological conditions and aerosol pollution levels.
 428



429
 430 **Figure 9.** Diurnal variations in ensemble mean coating depth ($D_{c,mean}$) on soot particles in different
 431 months for different particle sizes. Note that the color bars have different ranges of values in each
 432 panel.

433

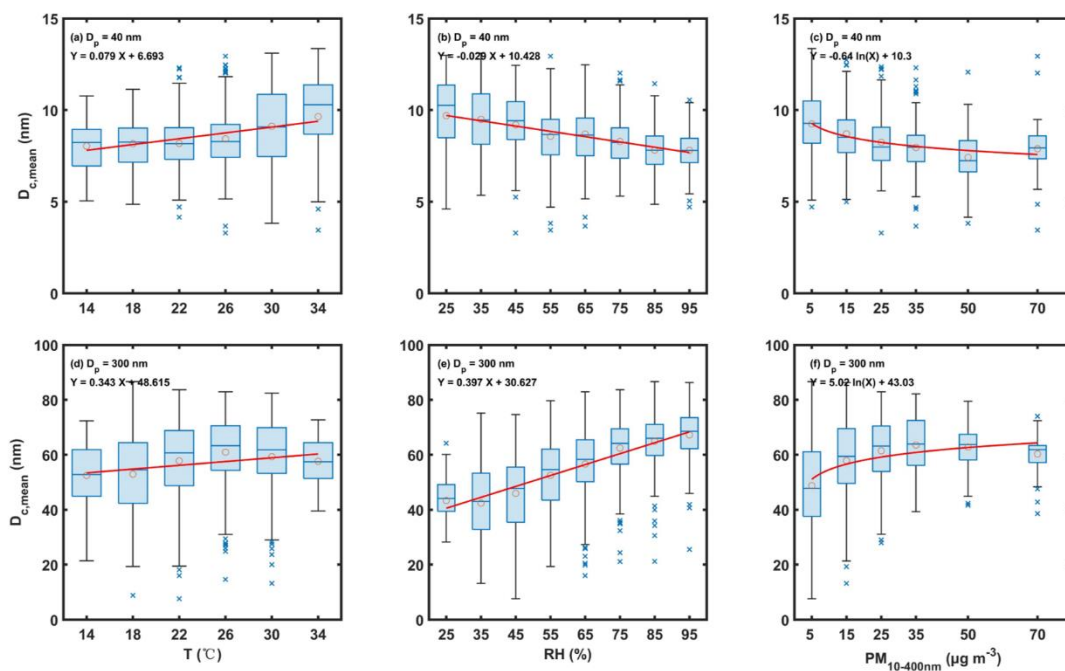
434 The relationships between $D_{c,mean}$ and several possible influencing factors (T , RH, and $PM_{10-400nm}$) were further analyzed (Fig. 10). Figures 10a and 10d show positive correlations between
 435 $D_{c,mean}$ and T for both nucleation-mode and accumulation-mode particles (represented by 40-nm and
 436 $D_{c,mean}$ and T for both nucleation-mode and accumulation-mode particles (represented by 40-nm and
 437 300-nm particles, respectively). This is consistent with the results shown in Fig. 7. Zhang et al.
 438 (2021) also indicated that warm environments were favorable to the aging of rBC . The high daytime
 439 T was conducive to the aging of soot particles caused by strong photochemical reactions. However,
 440 the relationships between RH and $D_{c,mean}$ (Figs. 9b and 9e) and between $PM_{10-400nm}$ and $D_{c,mean}$ (Figs.
 441 9c and 9f) were inverse between nucleation- and accumulation-mode soot particles.

442 Figure 9 depicts a linear relationship between $D_{c,mean}$ and RH, while a logarithmic relationship
 443 between $D_{c,mean}$ and $PM_{10-400nm}$. $D_{c,mean}$ in the nucleation mode decreased with increasing RH and
 444 $PM_{10-400nm}$ for nucleation-mode soot particles (Fig. 9b-c). This suggests that high ambient RH and
 445 severe aerosol pollution events could inhibit the coating of nucleation-mode soot particles. Previous
 446 studies have reported that aerosol pollution events were generally associated with high RH in the
 447 NCP (G. Wang et al., 2016; Z. Wu et al., 2018). This suggests that highly polluted environments
 448 with high ambient RH are not beneficial to the formation of new particles, leading to the weak
 449 coating on nucleation-mode soot particles. However, $D_{c,mean}$ in the accumulation mode increased
 450 with increasing RH and $PM_{10-400nm}$ (Fig. 9e-f). This suggests that highly polluted environments with
 451 high ambient RH favor the growth of accumulation-mode soot particles by coating. This is possibly

452 related to enhanced liquid-phase chemical reactions under these environmental conditions.
 453 Considering that accumulation-mode particles are the dominant components of $PM_{10-400nm}$, this
 454 further implies that the coating on soot particles is important to the formation of heavy aerosol
 455 pollution events. Y. Wang et al. (2019) indicated that the properties of ultrafine- and accumulation-
 456 mode particles were distinct in clean and polluted urban environments due to the different particle
 457 formation and growth processes. This study further indicates that it is also distinct in the aging of
 458 soot particles.

459 In summary, high ambient T and RH levels appeared to promote the coating growth of
 460 accumulation-mode soot particles in highly polluted environments. High ambient T but low RH
 461 were beneficial to the coating growth of nucleation-mode soot particles in less polluted
 462 environments.

463



464

465 **Figure 10.** Relationships between ensemble mean coating depth ($D_{c,mean}$) and ambient T (a, d) and
 466 RH (b, e), and $PM_{10-400nm}$ (c, f) for 40-nm (top panels) and 300-nm (bottom panels) particles. The
 467 circles show the mean $D_{c,mean}$ with boxes showing the 25th, 50th, and 75th percentiles and
 468 extremities show the 5th and 95th percentiles. Red lines show the linear or logarithmic fitting lines
 469 through the data, and best-fit relations are given in each panel.

470

471 4. Summary and conclusions

472 Soot particles containing most of the black carbon (BC) in the atmosphere are the most
 473 important light-absorbing carbonaceous particles. Investigating the mixing state of soot particles in

474 the field is crucial to accurately model aerosol absorption and reduce the uncertainty of radiative
475 forcing caused by aerosols in climate models.

476 Here, over five months of volatility tandem differential mobility analyzer (VTDMA) data
477 collected at a heavily polluted suburban site (Xingtai, or XT) from May to October of 2016 were
478 used to study the volatility and mixing state of size-resolved soot particles and their influencing
479 factors. Ambient meteorological variables [temperature (T), relative humidity (RH), and winds]
480 varied between the warm (June, July, and August) and cold (May, September, and October) months
481 of the field campaign. Variations in meteorological parameters could induce various aerosol aging
482 processes and different levels of aerosol pollution, largely impacting the volatility and mixing state
483 of soot particles.

484 The retrieved probability density function of the shrink factor (SF -PDF) at XT had three modes,
485 demonstrating that the volatility and mixing state of soot-containing particles were more complex
486 at XT than at other sites in the North China Plain. Compared with accumulation-mode soot-
487 containing particles, nucleation-mode soot-containing particles were more volatile and had a higher
488 degree of internal mixing. The diurnal variation patterns of SF -PDFs suggest that coating by newly
489 formed materials was the possible reason for the enhanced volatility of nucleation-mode soot-
490 containing particles in the daytime. Moreover, the enhanced nocturnal secondary aerosol formation
491 was responsible for the enhanced volatility of accumulation-mode soot-containing particles in the
492 nighttime. The ensemble mean SF (SF_{mean}) was size dependent and varied monthly. The monthly
493 variations in SF_{mean} became larger with increasing particle size, implying a stronger seasonal
494 variation of the coating effect on soot particles for larger-sized particles.

495 The similar diurnal variation trends of the number fraction of nonvolatile mode particles (NF_{NV})
496 in SF -PDFs and the mass concentration of BC (M_{BC}) suggest that human activities had a negative
497 influence on the volatility and degree of internal mixing of soot particles, especially for
498 accumulation-mode soot-containing particles. In general, less externally mixed soot particles (i.e.,
499 a smaller NF_{NV}) were present in warm months than in cold months. NF_{NV} was always lower in the
500 daytime than at night, suggesting a lower fraction of externally mixed soot particles in the daytime.
501 This suggests that daytime photochemical reactions may promote the transformation of externally
502 mixed soot particles into internally mixed soot particles. Moreover, NF_{NV} increased with increasing
503 particle size, meaning a higher degree of external mixing for larger-sized particles. This also
504 suggests that the degree of external mixing was higher for accumulation-mode soot particles than
505 for nucleation-mode soot particles.

506 To explore factors influencing soot-particle volatility and mixing state, the ensemble mean
507 coating depth ($D_{\text{c,mean}}$) of volatile matter on soot particles was investigated. $D_{\text{c,mean}}$ was thicker in
508 warm months than in cold months, even though aerosol pollution was heavier in cold months. In

509 warm months, $D_{c,mean}$ was larger in July than in other months, likely because high T , high RH, and
510 the stable atmospheric environment in July were conducive to the coating effect on soot particles.
511 The relationships between $D_{c,mean}$ and possible influencing factors (i.e., T , RH, and $PM_{10-400nm}$) show
512 that high ambient T and RH in a polluted environment promoted the coating growth of
513 accumulation-mode soot particles. High ambient T but low RH in a clean environment was
514 beneficial to the coating growth of nucleation-mode soot particles.

515 These results demonstrate great differences in the volatility and mixing state between nucleation-
516 and accumulation-mode soot particles. The impact of anthropogenic emissions on the volatility and
517 mixing state of soot-containing particles was clearly seen, especially for accumulation-mode soot-
518 containing particles. The monthly variations in meteorological conditions and aerosol pollution
519 levels may induce different aerosol aging processes, strongly impacting the volatility and mixing
520 state of soot-containing particles. This study suggests that differences between the mixing states of
521 nucleation- and accumulation-mode soot particles and their influencing factors should be considered
522 in climate models.

523
524 *Acknowledgement.* This work was funded by the National Natural Science Foundation of China
525 (NSFC) research project (grant no. 42030606, 42005067, 92044303), the National Key R&D
526 Program of the Ministry of Science and Technology, China (grant no. 2017YFC1501702), and the
527 Open Fund of State Key Laboratory of Remote Sensing Science (grant no. 202015). We also thank
528 all participants in the campaign for their tireless work and cooperation.

529
530 *Data availability.* The measurement data from the field experiment used in this study are available
531 from the first author upon request (yuyingwang@nuist.edu.cn).

532
533 *Author contributions.* YW conceived the study and led the overall scientific questions. YW,
534 RH, and QW processed the measurement data and prepared this paper. ZL, MC copyedited the
535 article. Other co-authors participated in the implementation of this experiment and the discussion
536 of this paper.

537
538 *Competing interests.* The authors declare that they have no conflict of interest.

539
540
541

542 **References**

- 543 Adachi, K., Sedlacek, A. J., Kleinman, L., Chand, D., Hubbe, J. M., and Buseck, P. R.: Volume changes
544 upon heating of aerosol particles from biomass burning using transmission electron microscopy,
545 *Aerosol Sci. Tech.*, 52, 46-56, <https://doi.org/10.1080/02786826.2017.1373181>, 2018.
- 546 Adachi, K., Sedlacek, A. J., Kleinman, L., Springston, S. R., Wang, J., Chand, D., Hubbe, J. M., Shilling,
547 J. E., Onasch, T. B., Kinase, T., Sakata, K., Takahashi, Y., and Buseck, P. R.: Spherical tarball
548 particles form through rapid chemical and physical changes of organic matter in biomass-burning
549 smoke, *Proceedings of the National Academy of Sciences*, 116, 19336-19341,
550 <https://doi.org/10.1073/pnas.1900129116>, 2019.
- 551 Bellouin, N., Quaas, J., Gryspeerdt, E., Kinne, S., Stier, P., Watson-Parris, D., Boucher, O., Carslaw, K.
552 S., Christensen, M., Daniau, A. L., Dufresne, J. L., Feingold, G., Fiedler, S., Forster, P., Gettelman,
553 A., Haywood, J. M., Lohmann, U., Malavelle, F., Mauritsen, T., McCoy, D. T., Myhre, G.,
554 Mülmenstädt, J., Neubauer, D., Possner, A., Rugenstein, M., Sato, Y., Schulz, M., Schwartz, S. E.,
555 Sourdeval, O., Storelvmo, T., Toll, V., Winker, D., and Stevens, B.: Bounding global aerosol radiative
556 forcing of climate change, *Rev. Geophys.*, 58, e2019R-e2660R, 2020.
- 557 Bond, T. C., Doherty, S. J., Fahey, D. W., Forster, P. M., Berntsen, T., DeAngelo, B. J., Flanner, M. G.,
558 Ghan, S., Kärcher, B., Koch, D., Kinne, S., Kondo, Y., Quinn, P. K., Sarofim, M. C., Schultz, M. G.,
559 Schulz, M., Venkataraman, C., Zhang, H., Zhang, S., Bellouin, N., Guttikunda, S. K., Hopke, P. K.,
560 Jacobson, M. Z., Kaiser, J. W., Klimont, Z., Lohmann, U., Schwarz, J. P., Shindell, D., Storelvmo, T.,
561 Warren, S. G., and Zender, C. S.: Bounding the role of black carbon in the climate system: A scientific
562 assessment, *J. Geophys. Res. Atmos.*, 118, 5380-5552, <https://doi.org/10.1002/jgrd.50171>, 2013.
- 563 Cheng, Y. F., Berghof, M., Garland, R. M., Wiedensohler, A., Wehner, B., Müller, T., Su, H., Zhang, Y.
564 H., Achtert, P., Nowak, A., Pöschl, U., Zhu, T., Hu, M., and Zeng, L. M.: Influence of soot mixing
565 state on aerosol light absorption and single scattering albedo during air mass aging at a polluted
566 regional site in northeastern China, *J. Geophys. Res. Atmos.*, 114, 2009.
- 567 Cheng, Y. F., Su, H., Rose, D., Gunthe, S. S., Berghof, M., Wehner, B., Achtert, P., Nowak, A.,
568 Takegawa, N., Kondo, Y., Shiraiwa, M., Gong, Y. G., Shao, M., Hu, M., Zhu, T., Zhang, Y. H.,
569 Carmichael, G. R., Wiedensohler, A., Andreae, M. O., and Pöschl, U.: Size-resolved measurement of
570 the mixing state of soot in the megacity Beijing, China: diurnal cycle, aging and parameterization,
571 *Atmos. Chem. Phys.*, 12, 4477-4491, 2012.
- 572 Cheung, H. H., Tan, H., Xu, H., Li, F., Wu, C., Yu, J. Z., and Chan, C. K.: Measurements of non-volatile
573 aerosols with a VTDMA and their correlations with carbonaceous aerosols in Guangzhou, China,
574 *Atmos. Chem. Phys.*, 16, 8431-8446, 2016.
- 575 Christensen, M., Gettelman, A., Cermak, J., Dagan, G., Diamond, M., Douglas, A., Feingold, G.,
576 Glassmeier, F., Goren, T., Grosvenor, D., Gryspeerdt, E., Kahn, R., Li, Z., Ma, P. L., Malavelle, F.,
577 McCoy, I., McCoy, D., McFarquhar, G., Mülmenstädt, J., Pal, S., Possner, A., Povey, A., Quaas, J.,
578 Rosenfeld, D., Schmidt, A., Schrödner, R., Sorooshian, A., Stier, P., Toll, V., Watson-Parris, D.,
579 Wood, R., Yang, M., and Yuan, T.: Opportunistic experiments to constrain aerosol effective radiative
580 forcing, *Atmos. Chem. Phys. Discuss.*, 2021, 1-60, 2021.
- 581 [Ehn, M., Thornton, J. A., Kleist, E., Sipilä, M., Junninen, H., Pullinen, I., Springer, M., Rubach, F.,](#)
582 [Tillmann, R., Lee, B., Lopez-Hilfiker, F., Andres, S., Acir, I., Rissanen, M., Jokinen, T.,](#)
583 [Schobesberger, S., Kangasluoma, J., Kontkanen, J., Nieminen, T., Kurtén, T., Nielsen, L. B.,](#)
584 [Jørgensen, S., Kjaergaard, H. G., Canagaratna, M., Maso, M. D., Berndt, T., Petäjä, T., Wahner, A.,](#)

585 [Kerminen, V., Kulmala, M., Worsnop, D. R., Wildt, J., and Mentel, T. F.: A large source of low-](#)
586 [volatility secondary organic aerosol, *Nature*, 506, 476-479, <https://doi.org/10.1038/nature13032>, 2014.](#)

587 Gustafsson, Ö., and Ramanathan, V.: Convergence on climate warming by black carbon aerosols, Proc.
588 Natl. Acad. Sci. U.S.A., 113, 4243, <https://doi.org/10.1073/pnas.1603570113>, 2016.

589 Hong, J., Äijälä, M., Häme, S. A. K., Hao, L., Duplissy, J., Heikkinen, L. M., Nie, W., Mikkilä, J.,
590 Kulmala, M., Prisle, N. L., Virtanen, A., Ehn, M., Paasonen, P., Worsnop, D. R., Riipinen, I., Petäjä,
591 T., and Kerminen, V. M.: Estimates of the organic aerosol volatility in a boreal forest using two
592 independent methods, *Atmos. Chem. Phys.*, 17, 4387-4399, [https://doi.org/10.5194/acp-17-4387-](https://doi.org/10.5194/acp-17-4387-2017)
593 2017, 2017.

594 Hossain, A. M. M. M., Park, S., Kim, J. S., and Park, K.: Volatility and mixing states of ultrafine particles
595 from biomass burning, *J. Hazard. Mater.*, 205-206, 189-197, 2012.

596 Hu, Z., Lu, Z., Zhang, H., Song, B., and Quan, Y.: Effect of oxidation temperature on oxidation reactivity
597 and nanostructure of particulate matter from a China VI GDI vehicle, *Atmos. Environ.*, 256, 118461,
598 <https://doi.org/10.1016/j.atmosenv.2021.118461>, 2021.

599 IPCC: Climate change 2021: The Physical Science Basis, sixth assessment of the Inter-governmental
600 Panel on Climate Change, 2021.

601 Kuniyal, J. C., and Guleria, R. P.: The current state of aerosol-radiation interactions: a mini review, *J.*
602 *Aerosol Sci.*, 130, 45-54, 2019.

603 La Rocca, A., Bonatesta, F., Fay, M. W., and Campanella, F.: Characterisation of soot in oil from a
604 gasoline direct injection engine using Transmission Electron Microscopy, *Tribol. Int.*, 86, 77-84,
605 <https://doi.org/10.1016/j.triboint.2015.01.025>, 2015.

606 Levy, M. E., Zhang, R., Khalizov, A. F., Zheng, J., Collins, D. R., Glen, C. R., Yuan, W., Yu, X. Y.,
607 Winston, L., and Jayne, J. T.: Measurements of submicron aerosols in Houston, Texas during the 2009
608 SHARP field campaign, *J. Geophys. Res. Atmos.*, 118, 10,518-10,534,
609 <https://doi.org/10.1002/jgrd.50785>, 2013.

610 Levy, M. E., Zhang, R., Zheng, J., Tan, H., Wang, Y., Molina, L. T., Takahama, S., Russell, L. M., and
611 Li, G.: Measurements of submicron aerosols at the California - Mexico border during the Cal-Mex
612 2010 field campaign, *Atmos. Environ.*, 88, 308-319, 2014.

613 Li, Z., Wang, Y., Guo, J., Zhao, C., Cribb, M. C., Dong, X., Fan, J., Gong, D., Huang, J., Jiang, M., Jiang,
614 Y., Lee, S. S., Li, H., Li, J., Liu, J., Qian, Y., Rosenfeld, D., Shan, S., Sun, Y., Wang, H., Xin, J., Yan,
615 X., Yang, X., Yang, X., Zhang, F., and Zheng, Y.: East Asian Study of Tropospheric Aerosols and
616 their Impact on Regional Clouds, Precipitation, and Climate (EAST-AIR_{CPC}), *J. Geophys. Res.*
617 *Atmos.*, 124, 13,026-13,054, <https://doi.org/10.1029/2019JD030758>, 2019.

618 Li, W. J., Zhang, D. Z., Shao, L. Y., Zhou, S. Z., and Wang, W. X.: Individual particle analysis of aerosols
619 collected under haze and non-haze conditions at a high-elevation mountain site in the North China
620 plain, *Atmos. Chem. Phys.*, 11, 11733-11744, 10.5194/acp-11-11733-2011, 2011.

621 Drinovec, L., Močnik, G., Zotter, P., Prévôt, A. S. H., Ruckstuhl, C., Coz, E., Rupakheti, M., Sciare, J.,
622 Müller, T., Wiedensohler, A., and Hansen, A. D. A.: The "dual-spot" Aethalometer: an improved
623 measurement of aerosol black carbon with real-time loading compensation, *Atmos. Meas. Tech.*, 8,
624 1965-1979, <https://doi.org/10.5194/amt-8-1965-2015>, 2015.

625 Novakov, T., Ramanathan, V., Hansen, J. E., Kirchstetter, T. W., Sato, M., Sinton, J. E., and Sathaye, J.
626 A.: Large historical changes of fossil-fuel black carbon aerosols, *Geophys. Res. Lett.*, 30,
627 <https://doi.org/10.1029/2002GL016345>, 2003.

628 Peng, J., Hu, M., Guo, S., Du, Z., Zheng, J., Shang, D., Zamora, M. L., Zeng, L., Shao, M., and Wu, Y.:

629 Markedly enhanced absorption and direct radiative forcing of black carbon under polluted urban
630 environments, *Proc. Natl. Acad. Sci. U.S.A.*, 113, 4266-4271, 2016.

631 Peng, J., Hu, M., Shang, D., Wu, Z., Du, Z., Tan, T., Wang, Y., Zhang, F., and Zhang, R.: Explosive
632 secondary aerosol formation during severe haze in the North China Plain, *Environ. Sci. Technol.*, 55,
633 2189-2207, <https://doi.org/10.1021/acs.est.0c07204>, 2021.

634 Philippin, S., Wiedensohler, A., and Stratmann, F.: Measurements of non-volatile fractions of pollution
635 aerosols with an eight-tube volatility tandem differential mobility analyzer (VTDMA-8), *J. Aerosol
636 Sci.*, 35, 185-203, <https://doi.org/10.1016/j.jaerosci.2003.07.004>, 2004.

637 Ramana, M. V., Ramanathan, V., Feng, Y., Yoon, S., Kim, S., Carmichael, G. R., and Schauer, J. J.:
638 Warming influenced by the ratio of black carbon to sulphate and the black-carbon source, *Nat. Geosci.*,
639 3, 542-545, <https://doi.org/10.1038/ngeo918>, 2010.

640 Ren, R., Li, Z., Yan, P., Wang, Y., Wu, H., Cribb, M., Wang, W., Jin, X., Li, Y., and Zhang, D.:
641 Measurement report: the effect of aerosol chemical composition on light scattering due to the
642 hygroscopic swelling effect, *Atmos. Chem. Phys.*, 21, 9977-9994, 2021.

643 Seinfeld, J. H., Bretherton, C., Carslaw, K. S., Coe, H., DeMott, P. J., Dunlea, E. J., Feingold, G., Ghan,
644 S., Guenther, A. B., Kahn, R., Kraucunas, I., Kreidenweis, S. M., Molina, M. J., Nenes, A., Penner, J.
645 E., Prather, K. A., Ramanathan, V., Ramaswamy, V., Rasch, P. J., Ravishankara, A. R., Rosenfeld,
646 D., Stephens, G., and Wood, R.: Improving our fundamental understanding of the role of aerosol-
647 cloud interactions in the climate system, *Proc. Natl. Acad. Sci. U.S.A.*, 113, 5781, 2016.

648 Stolzenburg, M. R., and McMurry, P. H.: TDMAFIT user's manual, University of Minnesota,
649 Department of Mechanical Engineering, Particle Technology Laboratory, Minneapolis, 1-61, 1988.

650 Stolzenburg, M. R., and McMurry, P. H.: Equations governing single and tandem DMA configurations
651 and a new lognormal approximation to the transfer function, *Aerosol Sci. Tech.*, 42, 421-432, 2008.

652 Swietlicki, E., Hansson, H. C., Hämeri, K., Svenningsson, B., Massling, A., Mcfiggans, G., McMurry, P.
653 H., Petäjä, T., Tunved, P., Gysel, M., Topping, D., Weingartner, E., Baltensperger, U., Rissler, J.,
654 Wiedensohler, A., and Kulmala, M.: Hygroscopic properties of submicrometer atmospheric aerosol
655 particles measured with H-TDMA instruments in various environments—a review, *Tellus B: Chem.
656 Phys. Meteor.*, 60, 432-469, <https://doi.org/10.1111/j.1600-0889.2008.00350.x>, 2008.

657 Twohy, C. H., Coakley Jr., J. A., and Tahnk, W. R.: Effect of changes in relative humidity on aerosol
658 scattering near clouds, *J. Geophys. Res. Atmos.*, 114, 2009.

659 Wang, G., Zhang, R., Gomez, M. E., Yang, L., Zamora, M. L., Hu, M., Lin, Y., Peng, J., Guo, S., and
660 Meng, J.: Persistent sulfate formation from London Fog to Chinese haze, *Proc. Natl. Acad. Sci. U.S.A.*,
661 113, 13,630-13,635, 2016.

662 Wang, J., Liu, D., Ge, X., Wu, Y., Shen, F., Chen, M., Zhao, J., Xie, C., Wang, Q., Xu, W., Zhang, J.,
663 Hu, J., Allan, J., Joshi, R., Fu, P., Coe, H., and Sun, Y.: Characterization of black carbon-containing
664 fine particles in Beijing during wintertime, *Atmos. Chem. Phys.*, 19, 447-458,
665 <https://doi.org/10.5194/acp-19-447-2019>, 2019.

666 Wang, Y., Zhang, F., Li, Z., Tan, H., Xu, H., Ren, J., Zhao, J., Du, W., and Sun, Y.: Enhanced
667 hydrophobicity and volatility of submicron aerosols under severe emission control conditions in
668 Beijing, *Atmos. Chem. Phys.*, 17, 5239-5251, <https://doi.org/10.5194/acp-17-5239-2017>, 2017.

669 Wang, Y., Li, Z., Zhang, Y., Du, W., Zhang, F., Tan, H., Xu, H., Fan, T., Jin, X., Fan, X., Dong, Z.,
670 Wang, Q., and Sun, Y.: Characterization of aerosol hygroscopicity, mixing state, and CCN activity at
671 a suburban site in the central North China Plain, *Atmos. Chem. Phys.*, 18, 11,739-11,752,

672 <https://doi.org/10.5194/acp-18-11739-2018>, 2018.

673 Wang, Y., Li, Z., Zhang, R., Jin, X., Xu, W., Fan, X., Wu, H., Zhang, F., Sun, Y., Wang, Q., Cribb, M.,
674 and Hu, D.: Distinct ultrafine- and accumulation-mode particle properties in clean and polluted urban
675 environments, *Geophys. Res. Lett.*, 46, 10,918-10,925, <https://doi.org/10.1029/2019GL084047>, 2019.

676 Wang, Y., Wang, J., Li, Z., Jin, X., Sun, Y., Cribb, M., Ren, R., Lv, M., Wang, Q., Gao, Y., Hu, R.,
677 Shang, Y., and Gong, W.: Contrasting aerosol growth potential in the northern and central-southern
678 regions of the North China Plain: implications for combating regional pollution, *Atmos. Environ.*,
679 267, 118723, <https://doi.org/10.1016/j.atmosenv.2021.118723>, 2021.

680 Wehner, B., Berghof, M., Cheng, Y. F., Achtert, P., Birmili, W., Nowak, A., Wiedensohler, A., Garland,
681 R. M., Pöschl, U., and Hu, M.: Mixing state of nonvolatile aerosol particle fractions and comparison
682 with light absorption in the polluted Beijing region, *J. Geophys. Res. Atmos.*, 114, 85-86, 2009.

683 Wu, Y., Wang, X., Tao, J., Huang, R., Tian, P., Cao, J., Zhang, L., Ho, K. F., Han, Z., and Zhang, R.:
684 Size distribution and source of black carbon aerosol in urban Beijing during winter haze episodes,
685 *Atmos. Chem. Phys.*, 17, 7965-7975, <https://doi.org/10.5194/acp-17-7965-2017>, 2017.

686 Wu, Z., Wang, Y., Tan, T., Zhu, Y., Li, M., Shang, D., Wang, H., Lu, K., Guo, S., Zeng, L., and Zhang,
687 Y.: Aerosol liquid water driven by anthropogenic inorganic salts: implying its key role in haze
688 formation over the North China Plain, *Environ. Sci. Tech. Lett.*, 5, 160-166,
689 <https://doi.org/10.1021/acs.estlett.8b00021>, 2018.

690 Zhang, F., Wang, Y., Peng, J., Chen, L., Sun, Y., Duan, L., Ge, X., Li, Y., Zhao, J., Liu, C., Zhang, X.,
691 Zhang, G., Pan, Y., Wang, Y., Zhang, A. L., Ji, Y., Wang, G., Hu, M., Molina, M. J., and Zhang, R.:
692 An unexpected catalyst dominates formation and radiative forcing of regional haze, *Proc. Natl. Acad.*
693 *Sci. U.S.A.*, 117, 3960, <https://doi.org/10.1073/pnas.1919343117>, 2020.

694 Yu, C., Liu, D., Broda, K., Joshi, R., Olfert, J., Sun, Y., Fu, P., Coe, H., and Allan, J. D.: Characterising
695 mass-resolved mixing state of black carbon in Beijing using a morphology-independent measurement
696 method, *Atmos. Chem. Phys.*, 20, 3645-3661, <https://doi.org/10.5194/acp-20-3645-2020>, 2020.

697 Zhang, S. L., Ma, N., Kecorius, S., Wang, P. C., Hu, M., Wang, Z. B., Größ, J., Wu, Z. J., and
698 Wiedensohler, A.: Mixing state of atmospheric particles over the North China Plain, *Atmos. Environ.*,
699 125, Part A, 152-164, <https://doi.org/10.1016/j.atmosenv.2015.10.053>, 2016.

700 Zhang, Y., Zhang, Q., Cheng, Y., Su, H., Kecorius, S., Wang, Z., Wu, Z., Hu, M., Zhu, T., Wiedensohler,
701 A., and He, K.: Measuring the morphology and density of internally mixed black carbon with SP2
702 and VTDMA: new insight into the absorption enhancement of black carbon in the atmosphere, *Atmos.*
703 *Meas. Tech.*, 9, 1833-1843, <https://doi.org/10.5194/amt-9-1833-2016>, 2016.

704 Zhang, Y., Du, W., Wang, Y., Wang, Q., Wang, H., Zheng, H., Zhang, F., Shi, H., Bian, Y., Han, Y., Fu,
705 P., Canonaco, F., Prévôt, A. S. H., Zhu, T., Wang, P., Li, Z., and Sun, Y.: Aerosol chemistry and
706 particle growth events at an urban downwind site in North China Plain, *Atmos. Chem. Phys.*, 18,
707 14,637-14,651, <https://doi.org/10.5194/acp-18-14637-2018>, 2018.

708 Zhang, Y., Liu, H., Lei, S., Xu, W., Tian, Y., Yao, W., Liu, X., Liao, Q., Li, J., Chen, C., Sun, Y., Fu, P.,
709 Xin, J., Cao, J., Pan, X., and Wang, Z.: Mixing state of refractory black carbon in fog and haze at
710 rural sites in winter on the North China Plain, *Atmos. Chem. Phys.*, 21, 17631-17648,
711 <https://doi.org/10.5194/acp-21-17631-2021>, 2021.

712 Zhou, C., Zhang, H., Zhao, S., and Li, J.: Simulated effects of internal mixing of anthropogenic aerosols
713 on the aerosol-radiation interaction and global temperature, *Int. J. Climatol.*, 37, 972-986, 2017.

714